

THE GROWTH OF H II REGIONS DURING REIONIZATION

STEVEN R. FURLANETTO¹, MATIAS ZALDARRIAGA^{2,3}, & LARS HERNQUIST²
Draft version December 2, 2024

ABSTRACT

Recently, there has been a great deal of interest in understanding the reionization of hydrogen in the intergalactic medium (IGM). One of the major outstanding questions is how this event proceeds on large scales. Motivated by numerical simulations, we develop a model for the growth of H II regions during the reionization era. We associate ionized regions with large-scale density fluctuations and use the excursion set formalism to model the resulting size distribution. We then consider ways in which to characterize the morphology of ionized regions. We show how to construct the power spectrum of fluctuations in the neutral hydrogen field. The power spectrum contains definite features from the H II regions which should be observable with the next generation of low-frequency radio telescopes through surveys of redshifted 21 cm emission from the reionization era. Finally, we also consider statistical descriptions beyond the power spectrum and show that our model of reionization qualitatively changes the distribution of neutral gas in the IGM.

Subject headings: cosmology: theory – intergalactic medium – diffuse radiation

1. INTRODUCTION

The reionization of the intergalactic medium (IGM) is one of the landmark events in early structure formation. It marks the epoch at which radiative feedback from luminous objects impacted the farthest reaches of the Universe – the point at which structure formation affected every baryon in the Universe, albeit indirectly. The timing, duration, and character of this event contain an enormous amount of information about the first cosmic structures and also have important implications for later generations of baryonic objects. For these reasons, a great deal of attention – both observational and theoretical – has recently been focused on this process. Most significantly, reionization is an important signpost that connects several disparate observations. Currently the data provide tantalizing hints about the ionization history of the Universe but few definitive answers. Observations of Ly α absorption in the spectra of high-redshift quasars indicate that reionization ends at $z \sim 6.5$ (Becker et al. 2001; Fan et al. 2002; White et al. 2003; Wyithe & Loeb 2004), although this interpretation is controversial (Songaila 2004). The main difficulty with these measurements is that the Ly α optical depth is extremely large in a fully neutral medium (Gunn & Peterson 1965), making it difficult to place strong constraints when the neutral fraction exceeds $\sim 10^{-3}$. On the other hand, measurements of the cosmic microwave background (CMB) imply a high optical depth to electron scattering, apparently requiring reionization to begin at $z \gtrsim 14$ (Kogut et al. 2003; Spergel et al. 2003). Unfortunately, the CMB data provide only an integral constraint on the ionization history. Taken together, these observations rule out simple pictures of fast reionization (e.g., Barkana & Loeb 2001 and references therein), but it is not yet clear what they do imply about early generations of luminous sources (Sokasian et al. 2003a,b; Wyithe & Loeb 2003; Cen 2003; Haiman & Holder 2003; Onken & Miralda-Escudé 2003; Fukugita & Kawasaki 2003).

At the same time, our theoretical understanding of how reionization proceeds, given some source population, has been advancing rapidly. Most models of reionization are based on the growth of H II regions around individual galaxies (Arons & Wingert 1972; Barkana & Loeb 2001). These models use semi-analytic techniques to compute the evolution of global quantities like the total ionized fraction. However, they are unable to describe the morphology of reionization, an issue that is both theoretically interesting and observationally accessible. Morphology is a difficult aspect to address because it depends on such factors as the locations of individual sources, the clumpiness of the IGM, the underlying density distribution (the cosmic web), recombinations, and radiative transfer effects. Some semi-analytic models have been developed to address these issues. The most popular assumes that reionization is controlled by recombinations and proceeds from low to high density regions (Miralda-Escudé et al. 2000), but these models are approximate at best. Fortunately, it has recently become possible to incorporate radiative transfer into numerical simulations of the reionization era (Gnedin 2000; Sokasian et al. 2003a,b; Ciardi et al. 2003), at least as a post-processing step. Because simulations can include all of the above processes (with the possible exception of clumpiness, which still requires extremely high mass resolution), they give a more nuanced view of the reionization process. One of the chief lessons of the simulations is that reionization is significantly more inhomogeneous than expected. The classical picture of a large number of small H II regions surrounding individual galaxies does not match the simulations well; instead, a relatively small number of large ionized regions appear around clusters of sources (see, for example, Figure 6 of Sokasian et al. 2003a). Moreover, in the simulations reionization proceeds from high to low density regions, implying that recombinations play only a secondary role in determining the morphology of reionization; instead, large-scale bias plays a dominant role. This picture suggests a new approach to analytic models of reionization, one that takes into account the large-scale density fluctuations that are ultimately responsible for this ionization pattern. We describe such a model in §2. We derive the size distribution of H II regions in a way analogous to the Press & Schechter (1974) halo mass function and show that it has the qualitative features seen in the

¹ Division of Physics, Mathematics, & Astronomy; California Institute of Technology; Mail Code 130-33; Pasadena, CA 91125; sfurlane@tapir.caltech.edu

² Harvard-Smithsonian Center for Astrophysics, 60 Garden St., Cambridge, MA 02138

³ Jefferson Laboratory of Physics, Harvard University, Cambridge, MA 02138

simulations.

Observing the morphology of H II regions requires new observational techniques as well as robust ways to characterize the data. Among the most exciting approaches to study the reionization process are surveys of 21 cm emission from neutral hydrogen at high redshifts (Field 1958; Scott & Rees 1990; Madau et al. 1997; Zaldarriaga et al. 2004). The idea behind these observations is to map the fluctuating pattern of emission (or absorption) from neutral hydrogen in the Universe over a range of frequencies. This yields a measurement of fluctuations due to both the density field and the H II regions. Because 21 cm emission comes from a single spectral line, such observations allow a three-dimensional reconstruction of the evolution of neutral hydrogen in the IGM and, owing to the design of low-frequency radio telescopes, can probe the large cosmological volumes needed to study the IGM. Despite numerous technical challenges, instruments able to make the necessary observations will be built in the coming years. These include the Primeval Structure Telescope (*PAST*),⁴ the Low Frequency Array (*LOFAR*),⁵ and the Square Kilometer Array (*SKA*).⁶ The major obstacles to high-redshift 21 cm observations are the many bright foreground sources, which include Galactic synchrotron emission, free-free emission from galaxies (Oh & Mack 2003), faint radio-loud quasars (Di Matteo et al. 2002), and synchrotron emission from low-redshift galaxy clusters (Di Matteo et al. 2004). Fortunately, all of these foregrounds have smooth continuum spectra. Zaldarriaga et al. (2004; hereafter ZFH04) showed that the foregrounds can be removed to high precision because the 21 cm signal itself is uncorrelated over relatively small frequency ranges. ZFH04 also showed how to compute the angular power spectrum of the 21 cm sky as a function of frequency, given some model of reionization. This is the simplest statistical measure of the morphology of H II regions, and they showed that it is quite powerful in distinguishing different stages of reionization (at least in a simple toy model).

Of course, predictions for the 21 cm signal, or any other measurement of reionization, rely on an accurate model for reionization. The initial conditions are straightforward: when the neutral fraction $\bar{x}_H \approx 1$, the power spectrum follows that of the density (Tozzi et al. 2000). This breaks down when the H II regions appear, and more sophisticated approaches become necessary. There have been several recent attempts to predict the signal using numerical simulations (Ciardi & Madau 2003; Furlanetto et al. 2004a; Gnedin & Shaver 2003). However, the boxes in these simulations have sizes $\lesssim 20$ Mpc, subtending only a few arcminutes on the sky. Because the angular resolution of low frequency radio telescopes at the required sensitivity is also a few arcminutes (ZFH04), such predictions require extrapolations to larger scales, which may be dangerous given the already large sizes of ionized regions. With our analytic model for the size distribution of these bubbles, we are able to make the first detailed statistical characterizations of the fluctuating ionization pattern on the large scales most relevant to observations. We begin with the power spectrum as the simplest description. In §3, we show how to compute the power spectrum for an arbitrary size distribution, and in §4 we apply that formalism to our model of H II regions.

The power spectrum is only one way to describe the 21 cm

⁴ See <http://astrophysics.phys.cmu.edu/~jbp> for details on *PAST*.

⁵ See <http://www.lofar.org> for details on *LOFAR*.

⁶ See <http://www.skatelescope.org> for details on the *SKA*.

field. It is an excellent approximation if fluctuations in the matter density dominate the signal, because the density field is nearly gaussian on the large scales of interest here. Unfortunately, once the H II regions dominate the power spectrum, the probability distribution is no longer gaussian (Morales & Hewitt 2003). There have, however, been no attempts to describe the distribution. Using our model for reionization, we discuss some of the relevant features in §5. We show that the reionization model qualitatively changes the character of fluctuations in the neutral gas density.

This paper is primarily concerned with developing a general and useful model for the morphology of reionization and with the crucial features of that model. We will focus here on the physics of reionization rather than on their observable consequences; we consider some of these in a companion paper about the 21 cm signal expected from high redshifts (Furlanetto et al. 2004b).

In our numerical calculations, we assume a cosmology with $\Omega_m = 0.3$, $\Omega_\Lambda = 0.7$, $\Omega_b = 0.046$, $H = 100h \text{ km s}^{-1} \text{ Mpc}^{-1}$ (with $h = 0.7$), $n = 1$, and $\sigma_8 = 0.9$, consistent with the most recent measurements (Spergel et al. 2003).

2. H II REGIONS DURING REIONIZATION

In this section, we will calculate the size distribution of ionized regions within the IGM. So long as ultraviolet photons are responsible for reionization, it is a good approximation to divide the IGM into a fully neutral component inside of which sit discrete, fully ionized bubbles. We will make this approximation throughout; we consider some more complicated cases in Furlanetto et al. (2004b). A complete description requires accurately locating the ionizing sources, fully resolving the clumpiness of the IGM, following recombinations, and performing radiative transfer. These problems all require numerical simulations (e.g., Gnedin 2000; Sokasian et al. 2003a,b; Ciardi et al. 2003 and references therein). As a result, semi-analytic models have avoided this question and focused on global quantities such as the mean neutral fraction \bar{x}_H . The simplest semi-analytic model, and the usual assumption in the literature, is to associate each ionized region with a single galaxy (e.g., Barkana 2002; Loeb et al. 2004). In this case the size distribution dn/dm (where m is the mass of the ionized region) follows directly from the halo mass function if we make the simple ansatz that

$$m_{\text{ion}} = \zeta m_{\text{gal}}, \quad (1)$$

where m_{gal} is the mass in a collapsed object and ζ is some efficiency factor. It could, for example, be written $\zeta = f_{\text{esc}} f_* N_{\gamma/b} n_{\text{rec}}^{-1}$, with f_{esc} the escape fraction of ionizing photons from the object, f_* the star formation efficiency, $N_{\gamma/b}$ the number of ionizing photons produced per baryon in stars, and n_{rec} the typical number of times a hydrogen atom has recombined. These parameters all depend on the uncertain source properties and can be functions of time; we will consider several possible values for ζ below.

Because the mass function is steep at high redshifts, the resulting H II regions are quite small (see the discussion of Figure 4 below). This conflicts with even the most basic pictures from simulations (Sokasian et al. 2003a; Ciardi et al. 2003). “Typical” ionized regions in simulations extend to several comoving Mpc in radius even early in overlap, many times larger than Strömgren spheres around individual galaxies. The reason is simply that the Strömgren spheres of nearby protogalaxies add, so that biased regions tend to host surprisingly large ionized regions. For example, Figure 6 of

Sokasian et al. (2003a) shows that H II regions tend to grow around the largest clusters of sources, in this case primarily along filaments. In fact, the radius of the H II regions quickly exceeds the correlation length of galaxies, so it is difficult to see how to construct a model for the bubbles based on “local” galaxy properties.

Therefore, in order to describe the neutral fraction field, x_H , we need to take into account large-scale fluctuations in the density field. Here we describe a simple way to do so. We again begin with the ansatz of equation (1) and ask whether an isolated region of mass m is *fully* ionized or not. Because it is isolated, the region must contain enough mass in luminous sources to ionize all of its hydrogen atoms; thus we can impose a condition on the collapse fraction:

$$f_{\text{coll}} \geq f_x \equiv \zeta^{-1}. \quad (2)$$

In the extended Press-Schechter model (Bond et al. 1991; Lacey & Cole 1993), the collapse fraction is a deterministic function of the mean linear overdensity δ_m of our region:

$$f_{\text{coll}} = \text{erfc} \left[\frac{\delta_c(z) - \delta_m}{\sqrt{2[\sigma_{\min}^2 - \sigma^2(m)]}} \right], \quad (3)$$

where $\sigma^2(m)$ is the variance of density fluctuations on the scale m , $\sigma_{\min}^2 = \sigma^2(m_{\min})$, $\delta_c(z)$ is the critical density for collapse, and m_{\min} is the minimum mass of an ionizing source⁷. Unless otherwise specified, we will take m_{\min} to be the mass corresponding to a virial temperature of 10^4 K, at which atomic hydrogen line cooling becomes efficient. Note that this expression assumes that the mass fluctuations are gaussian on the scale m ; the formula thus begins to break down when we consider mass scales close to the typical size of collapsed objects. Armed with this result, we can rewrite condition (2) as a constraint on the density:

$$\delta_m \geq \delta_x(m, z) \equiv \delta_c(z) - \sqrt{2}K(\zeta)[\sigma_{\min}^2 - \sigma^2(m)]^{1/2}, \quad (4)$$

where $K(\zeta) = \text{erf}^{-1}(1 - \zeta^{-1})$. We see that regions with sufficiently large overdensities will be able to “self-ionize.”

In order to compute the size distribution of ionized regions we must overcome two additional, but related, difficulties. First, we apparently must settle on an appropriate smoothing scale m . Second, we must take into account ionizing photons from galaxies *outside* of the region under consideration. In other words, an underdense void m_1 may be ionized by a neighboring cluster of sources in an overdense region m_2 provided that the cluster has enough “extra” ionizing photons. But notice that we can solve the latter problem by changing our smoothing scale to $m_1 + m_2$: then the net collapse fraction in this region would be large enough to “self-ionize.”

This suggests that we wish to assign a point in space to an ionized region of mass m if and only if the scale m is the *largest* scale for which condition (4) is fulfilled. If this procedure can be done self-consistently, we will not need to arbitrarily choose a smoothing scale. Our problem is analogous to constructing the halo mass function through the excursion set formalism (Bond et al. 1991): starting at $m = \infty$, we move to smaller scales surrounding the point of interest and compute the smoothed density field as we go along. Once $\delta_m = \delta_x(m, z)$,

⁷ Note that in equation (3) the growth of structure is encoded in the time evolution of $\delta_c(z)$, with $\sigma^2(m)$ constant in time. We adopt this convention in the rest of the paper.

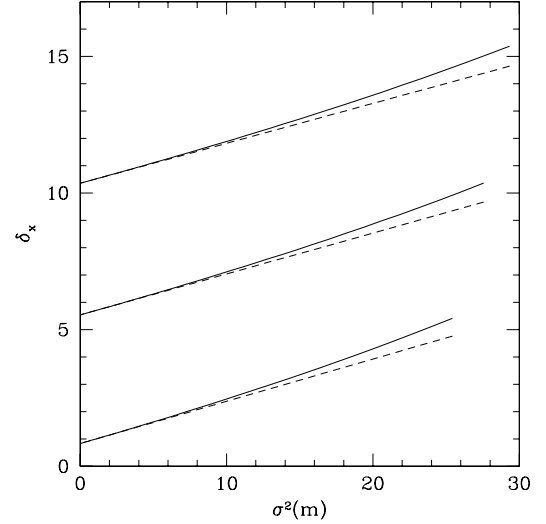


FIG. 1.— The density threshold $\delta_x(\sigma^2, z)$ at several different redshifts, assuming $\zeta = 40$. The curves are for $z = 20, 16$, and 12 , from top to bottom. Within each set, the solid curve is the true $\delta_x(m, z)$ and the dashed line is the fit $B(m, z)$.

we have identified a region with enough sources to ionize itself, and we assign these points to objects of the appropriate mass. To obtain the mass function, we need to find the distribution of first up-crossings above the curve described by δ_x . (We are concerned only with the first-crossing distribution because those trajectories that later wander below the barrier correspond to regions ionized by sources in neighboring volumes.) Again, we need not choose a smoothing scale; each point is *assigned* to an object of mass m based on its own behavior.

The solid lines in Figure 1 show the barrier $\delta_x(m, z)$ for several redshifts as a function of $\sigma^2(m)$. In each case the curves end at $\sigma^2(\zeta m_{\min})$; this is the minimum size of an H II region in our formalism. The Figure shows an important difference between our problem and the excursion set formalism applied to the halo mass function. In the latter case, the barrier $\delta_c(z)$ is independent of mass. Clearly this would not be a good approximation in our case. Unfortunately, there is no general method for constructing the first-crossing distribution above a barrier of arbitrary shape (but see Sheth & Tormen [2002] for an approximate method). The most complicated case for which an analytic solution is available is a linear barrier (Sheth 1998). The dashed curves in Figure 1 show linear “fits” to the barrier constructed in the following way. First note that, as $m \rightarrow \infty$,

$$\delta_x \rightarrow B_0 \equiv \delta_c(z) - \sqrt{2}K(\zeta)\sigma_{\min}. \quad (5)$$

Also, at any given σ^2 , the slope is simply

$$\frac{\partial \delta_x}{\partial \sigma^2} = \frac{K(\zeta)}{\sqrt{2(\sigma_{\min}^2 - \sigma^2)}}. \quad (6)$$

We define B_1 to be this slope evaluated at $\sigma^2 = 0$. The dashed lines in Figure 1 are $B(m, z) = B_0 + B_1 \sigma^2(m)$, i.e. a linear fit to the true barrier at $m = \infty$. We see that this is a reasonable approximation to the true barrier shape for σ^2 that are not too large. The fit departs from δ_x as the mass approaches the size of H II regions around individual galaxies. However, equation (3) – upon which the entire approach is predicated – also

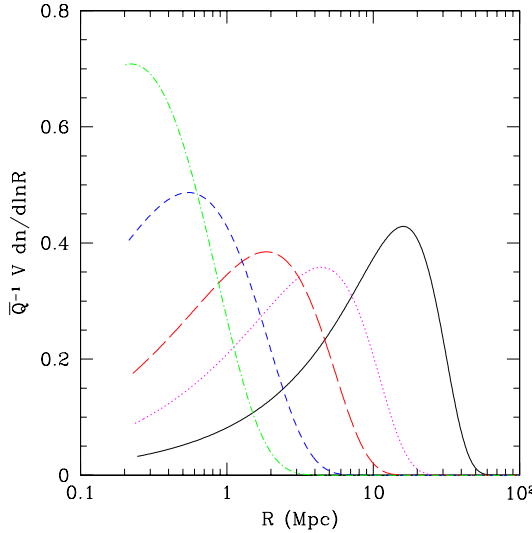


FIG. 2.— The bubble size distribution $\bar{Q}^{-1} V dn/d\ln R$ at several different redshifts in our model, assuming $\zeta = 40$ (note that R is the comoving size). Dot-dashed, short-dashed, long-dashed, dotted, and solid lines are for $z = 18, 16, 14, 13$, and 12 , respectively. These have $\bar{Q} = 0.037, 0.11, 0.3, 0.5$, and 0.74 .

breaks down on small mass scales. Thus we do not consider it necessary to improve the fit. (In any case, changing the slope of the barrier to fit $\sigma^2(\zeta m_{\min})$ exactly does not significantly change our results except at early times, when the bubbles are still quite rare.)

The advantage of a linear fit is that we can now write the mass function analytically (Sheth 1998):

$$m \frac{dn}{dm} = \sqrt{\frac{2}{\pi}} \frac{\bar{\rho}}{m} \left| \frac{d \ln \sigma}{d \ln m} \right| \frac{B_0}{\sigma(m)} \exp \left[-\frac{B^2(m, z)}{2\sigma^2(m)} \right]. \quad (7)$$

This is the comoving number density of H II regions with masses in the range $(m, m+dm)$. Figure 2 shows the resulting size distributions at several redshifts for $\zeta = 40$. The dot-dashed, short-dashed, long-dashed, dotted, and solid curves correspond to $z = 18, 16, 14, 13$, and 12 , respectively. The curves begin at the radius corresponding to an H II region around a galaxy of mass m_{\min} . We have normalized each curve by the fraction of space \bar{Q} filled by the bubbles,

$$\bar{Q} = \int dm \frac{dn}{dm} V(m), \quad (8)$$

where $V(m)$ is the comoving volume of a bubble of mass m . We show the evolution of \bar{Q} for several choices of ζ by the solid lines in Figure 3; the curves in Figure 2 range from $\bar{Q} = 0.037$ to $\bar{Q} = 0.74$. When the ionized fraction is small, the ionized regions are also small, with characteristic sizes $\lesssim 0.5$ Mpc. At this point they are not much bigger than the Strömgren spheres surrounding individual galaxies. However, the size increases rapidly as the neutral fraction decreases; when $\bar{Q} = 0.5$, the bubbles are already several Mpc in size. The characteristic scale then begins to increase extremely rapidly because $B_0 \rightarrow 0$ as we approach overlap (see Figure 1). This behavior matches the results of the simulations cited above – although note that the scales we find can exceed the simulation box sizes well before overlap (see below).

This contrasts sharply with a scenario in which we assign ionized regions to individual galaxies: the top panel of Figure

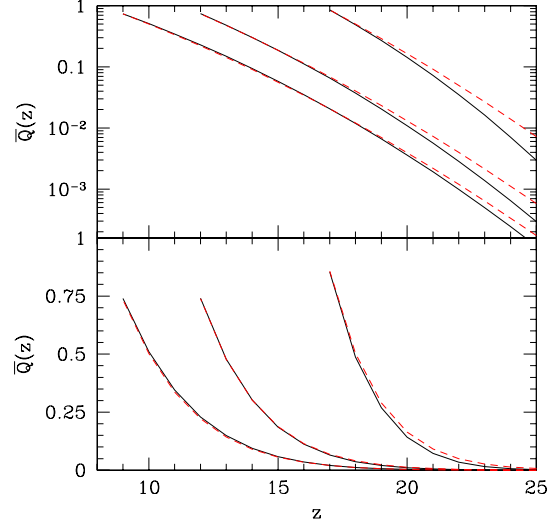


FIG. 3.— The global ionization history for several scenarios. The curves that rise from zero assume $\zeta = 500, 40$, and 12 , from right to left; solid lines are for our model and dashed lines are the “true” values, ζf_{coll} .

4 compares the predictions of our model with one in which each galaxy hosts its own distinct ionized bubble. Note that we have not normalized the curves by \bar{Q} . In the galaxy-based model, we see that the bubble sizes change only very slowly; the filling factor is dominated by the smallest galaxies. In such a scenario, overlap is achieved not by the growth of existing H II regions but through the formation of more distinct bubbles. Also note that, provided our model is correct, the sizes of ionized regions cannot be determined even from the Strömgren spheres around “large” or L_* galaxies. Instead large-scale fluctuations are *required* in order to understand the bubble pattern. The disparity between the models clearly increases rapidly as we approach overlap, but it is significant even at early times.

The mass function of ionized regions has qualitatively different behavior from the usual halo mass function. The most significant difference is that it has both low and high mass cutoffs. This occurs because the barrier rises more steeply than $\sigma(m)$, and it becomes harder for a trajectory to cross it at small masses (Sheth & Tormen 2002).⁸ As a result, the mass function has a characteristic scale that becomes sharper as \bar{Q} increases. In general, our model is good news for attempts to constrain the H II regions observationally. It predicts large features with a characteristic scale, which should make the ionized bubbles easier to identify.

Although we have argued that the general properties of our model reproduce the qualitative features found in simulations, we have not performed a quantitative comparison. This will clearly require a large simulation box in order to reproduce the size distribution we expect. In our model, the bubble sizes are essentially set by large-scale fluctuations of the density field; as emphasized by Barkana & Loeb (2003), the finite simulation size will bias these fluctuations and reduce the characteristic sizes. A numerical simulation typically forces $\delta = 0$ on the size scale of the box, L_{box} . We can calculate the expected size distribution in a box of the appropriate size by changing

⁸ Note that the real barrier rises more quickly than our linear approximation. This will make the low mass cutoff occur slightly earlier, increasing the sharpness of the peak in the size distribution.

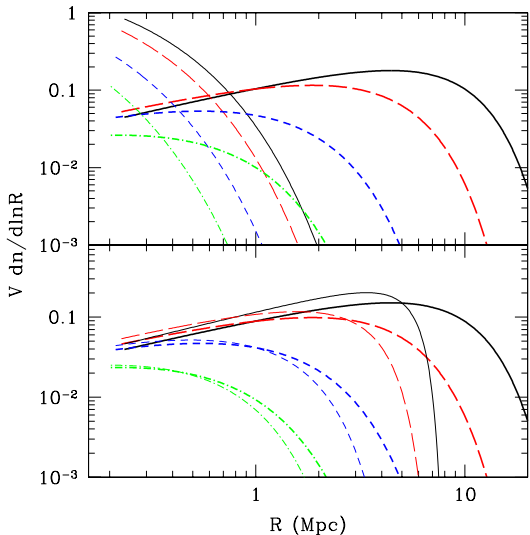


FIG. 4.— The bubble size distribution $V dn/d \ln R$ at several different redshifts, assuming $\zeta = 40$. In both panels, the thick lines show our model with dot-dashed, short-dashed, long-dashed, and solid lines corresponding to $z = 18, 16, 14$, and 13 , respectively. In the top panel, the thin lines assume individual galaxies source distinct H II regions. In the bottom panel, the thin lines use equation (9), with $L_{\text{box}} = 10h^{-1} \text{ Mpc} = 14.3 \text{ Mpc}$.

the origin of the excursion set formalism from $(\sigma^2 = 0, \delta = 0)$ to $(\sigma^2 = \sigma_{\text{box}}^2, \delta = 0)$. The results are exactly analogous to the extended Press-Schechter formalism for calculating conditional halo mass functions (Lacey & Cole 1993; Sheth & Tormen 2002); the size distribution is

$$m \frac{dn}{dm} \Big|_{\text{box}} = \sqrt{\frac{2}{\pi}} \frac{\bar{\rho}}{m} \left| \frac{d \ln \sigma}{d \ln m} \right| \frac{\sigma^2(m)}{[\sigma^2(m) - \sigma_{\text{box}}^2]^{3/2}} \times B_0 \exp \left[-\frac{B^2(M, z)}{2[\sigma^2(m) - \sigma_{\text{box}}^2]} \right]. \quad (9)$$

The results are compared to the “true” size distribution in the bottom panel of Figure 4, assuming $L_{\text{box}} = 10h^{-1} \text{ Mpc} = 14.3 \text{ Mpc}$; this is the same size as the simulations discussed by Sokasian et al. (2003a), which are among the largest volumes that have been used in numerical studies of reionization. We see that even state of the art simulations probably underestimate the sizes of ionized regions, especially during the late stages of overlap. Studying these epochs will require box sizes $\gtrsim 100 \text{ Mpc}$ for a fair sample.

Before proceeding to discuss the statistical properties of this distribution in more detail, we pause to note several caveats about our model. First, we do not necessarily have $Q = \zeta f_{\text{coll}}$, and hence our normalization may be incorrect. One reason is that equation (3) breaks down on sufficiently small scales. Also, we use the linear fit $B(m, z)$ rather than the true $\delta_x(m, z)$. We therefore expect that our model will not properly normalize the size distribution when the characteristic bubble size is small. Figure 3 indicates that this is indeed the case; the dashed curves (which give the true ionized fraction) lie significantly above the solid lines of our model at early times (when the bubbles are small). To solve this problem, we multiply our number densities by $\zeta f_{\text{coll}}/\bar{Q}$. Fortunately, the figure also shows that this correction becomes negligible when $\bar{Q} \gtrsim 0.1$. Thus the correction is only necessary when the bubbles have a small effect anyway. The required renormalization does increase if m_{min} increases (because equation

[3] breaks down sooner) but is never more than $\sim 20\%$ in the results we show.

Another caveat is that the excursion set formalism is fundamentally Lagrangian: it follows *mass elements* rather than *volume elements*. More massive regions will have expanded less than their underdense neighbors. We do not include this difference in calculating the radial sizes of the regions; this is reasonable because regions that cross our barriers are still far from turnaround at these early times. Moreover, we of course assume spherical H II regions: in reality they have much more complex shapes.

Finally, we emphasize several simplifications we have made to the physics of reionization. First, equation (1) neglects the environmental dependence of the ionizing efficiency. The recombination rate, for example, increases with the mean local density, making ζ a function of the density. It is possible to formulate a model of reionization based on the variation of the recombination rate with density (Miralda-Escudé et al. 2000); in such a model, low density voids are ionized first. However, the simulations show instead that the densest regions tend to be ionized first, at least if the sources are relatively faint and numerous (Sokasian et al. 2003a; Ciardi et al. 2003), in accord with our model. The basic reason is that high-redshift galaxies are strongly biased, so their abundance increases faster than the local density. Thus H II regions first appear in the densest regions and only then escape into the voids. Because subsequent generations of sources also form primarily in the dense regions, this structure is preserved throughout the ionization process. We compare our model to one in which voids are ionized first in Furlanetto et al. (2004b).

Recombinations will nevertheless be important in the detailed ionization pattern inside of each ionized region. Our model assumes that such regions are *fully* ionized; in reality, they will have a complex ionization pattern determined by recombinations in clumpy regions, “shadowing” of ionizing sources by high-column density objects, and the sheets and filaments of the cosmic web. In what follows, we ignore these complications, because they will imprint signatures into e.g. the angular power spectrum on scales much smaller than those characteristic of the bubbles as a whole.

3. CONSTRUCTING THE POWER SPECTRUM

We will now consider how to construct observable statistical measures of the size distribution of H II regions. If high signal-to-noise measurements are possible, then of course dn/dm of the ionized regions can be measured directly. We will instead consider regimes in which the H II regions cannot be mapped in detail but in which the fluctuation pattern can still be measured statistically. We will take as an example the 21 cm power spectrum (ZFH04). The fundamental observable in 21 cm measurements is the brightness temperature of the IGM (Field 1959; Madau et al. 1997),

$$\delta T_b \approx 23 \psi \times \left(\frac{T_S - T_{\text{CMB}}}{T_S} \right) \left(\frac{\Omega_b h^2}{0.02} \right) \times \left[\left(\frac{0.15}{\Omega_m h^2} \right) \left(\frac{1+z}{10} \right) \right]^{1/2} \text{ mK.} \quad (10)$$

Here, T_S is the hydrogen spin temperature and $\psi = x_H(1 + \delta)$, where x_H is the local neutral fraction and δ is the local overdensity; the other symbols have their usual meanings. We will assume throughout that $T_S \gg T_{\text{CMB}}$, so that δT_b is independent of the spin temperature; this is expected to be a good assumption soon after ionizing sources turn on (see ZFH04 for a more detailed discussion).

The simplest statistical description of the 21 cm field is provided by the power spectrum of ψ . In this section we will describe how to construct this function. We will find it simpler to work in terms of the correlation function ξ_ψ , which can be constructed explicitly from its component fields (ZFH04):

$$\xi_\psi = \xi_{xx}(1 + \xi_{\delta\delta}) + \bar{x}_H^2 \xi_{\delta\delta} + \xi_{x\delta}(2\bar{x}_H + \xi_{x\delta}). \quad (11)$$

Here ξ_{xx} is the correlation function of x_H , $\xi_{\delta\delta}$ is the correlation function of the density field, and $\xi_{x\delta}$ is the cross-correlation between the two fields. The power spectrum P_ψ is then the Fourier transform of this quantity. First, note that $\xi_{\delta\delta}$ can be obtained directly using standard techniques such as the halo model (e.g., Cooray & Sheth 2002). This includes nonlinear corrections to the power spectrum, although these are generally not important on the scales of interest. Because the x_H field is actually composed of isolated ionized regions, we find it more intuitive to work in terms of the correlation function of the ionized fraction, x_i . However, note that by linearity the two correlation functions are identical. In the following sections we describe how to build our model for ξ_{xx} . We first describe the necessary limits of the correlation function in §3.1 and explain why the simplest models fail. We go on to show how to compute ξ_{xx} for a randomly distributed set of H II regions in §3.2 and then how to add source clustering in §3.3. Finally, we compute $\xi_{x\delta}$ in §3.4. Note that we will neglect redshift space distortions and Jeans smoothing of the baryonic fluctuations.

3.1. Restrictions on ξ_{xx}

We expect the joint probability distribution to have the form (ZFH04)

$$\langle x_1 x_2 \rangle \equiv \langle x_i(\mathbf{r}_1) x_i(\mathbf{r}_2) \rangle = \bar{x}_i^2 + (\bar{x}_i - \bar{x}_i^2) f(r_{12}/R), \quad (12)$$

with $r_{12} = |\mathbf{r}_1 - \mathbf{r}_2|$ and R some characteristic bubble size. The function f has the limits $f \rightarrow 0$ for $r_{12} \gg R$ and $f \rightarrow 1$ as $r_{12} \rightarrow 0$. That is, if two points are separated by a distance much smaller than the size of a typical H II region they will either both be ionized by the same bubble, with probability \bar{x}_i , or both neutral. But if they are well-separated relative to the bubble size they must reside in distinct H II regions, and the probability approaches \bar{x}_i^2 . The correlation function is then $\xi_{xx} = \langle x_1 x_2 \rangle - \bar{x}_i^2$.

In addition, we must note that x_i can take values only in a restricted range from zero to unity. This means that $\bar{x}_i = 1$ implies $x_i = 1$ *everywhere*, so that the correlations vanish. Thus, we need $\xi_{xx} = 0$ when both $\bar{x}_i = 0$ and $\bar{x}_i = 1$. We note that this limit is not satisfied by many simple models. For example, Santos et al. (2003) argue that $\xi_{xx} \propto x_i^2 \xi_{\delta\delta}$ times some filter function that damps fluctuations inside the bubbles; this form does not have the correct limiting behavior. Santos et al. (2003) instead enforce the limit by choosing the bubble size to approach infinity at overlap (however, it does not have the correct behavior on large scales when $x_i < 1$). We require a prescription that self-consistently satisfies the above limit, independent of our prescription for bubble sizes. For example, we wish to contrast the model described in §2, in which the individual bubble sizes approach infinity at overlap, with other models in which overlap is achieved by increasing the number density of bubbles but not their sizes (such as placing H II regions around each galaxy; see Figure 4).

3.2. A Model for ξ_{xx}

Assuming that the sources are uncorrelated, the probability of having N sources in a volume V follows a Poisson distribution. Thus the probability that at least one source falls into this region is $1 - e^{-nV}$, where n is the number density of sources. We begin by assuming that all the bubbles have the same size V_I . The proper definition of the ionized fraction is

$$\bar{x}_i = 1 - e^{-nV_I} = 1 - e^{-\bar{Q}} \quad (13)$$

We let $V_o(r)$ be the volume of the overlap region between two ionized regions centered a distance r apart. The probability that both \mathbf{r}_1 and \mathbf{r}_2 are ionized has two parts. One possibility is that a single source can ionize both points if it is inside $V_o(r_{12})$. Alternatively, two separate sources can ionize the two points. The total joint probability is then

$$\langle x_1 x_2 \rangle = (1 - e^{-nV_o}) + e^{-nV_o} [1 - e^{-n(V_I - V_o)}]^2, \quad (14)$$

where $V_o \equiv V_o(r_{12})$. One can easily verify that the formula obeys all of the restrictions described in §3.1.

We now wish to relax the assumption of a single bubble size; we will index the bubble size with m for reasons that are probably obvious. We first calculate the probability that a given point is ionized. Around that point, there is a sphere of radius $R(m_1)$ where even the smallest allowed source (with index m_1) is able to ionize the point. Let P_1 be the probability that this occurs. If that does not happen, there is a shell surrounding this sphere in which a source of radius $R(m_2)$ can ionize our point; let P_2 be the probability of there being a source of large enough size in this region. If this does not happen, there is another shell in which a source of radius $R(m_3)$ can ionize the point, etc. We can write the total probability \bar{x}_i that the point is ionized as

$$\begin{aligned} \bar{x}_i &= P_1 + (1 - P_1)P_2 + (1 - P_1)(1 - P_2)P_3 + \dots \\ &= 1 - \exp \left[\sum_m \ln(1 - P_m) \right] \\ &= 1 - \exp \left[\sum_m n(m)V(m) \right], \end{aligned} \quad (15)$$

where $n(m)$ is the number density of sources with index m .

The correlation function can be calculated in the same way as above. One possibility is that the two points are ionized by the same source; this requires at least one source of size m to be in the appropriate overlap region $V_o(m)$. The probability for this to occur is

$$P(1 \text{ source}) = 1 - \exp \left[\sum_m n(m)V_o(m) \right]. \quad (16)$$

The other possibility is that the points are ionized by different sources. Again there is a succession of regions, this time of size $V(m) - V_o(m)$, where a source of size m can ionize one point but not the other. Thus [c.f. equation (14)]

$$\begin{aligned} \langle x_1 x_2 \rangle &= \left\{ 1 - \exp \left(- \int dm \frac{dn}{dm} V_o(m) \right) \right\} \\ &\quad + \exp \left(- \int dm \frac{dn}{dm} V_o(m) \right) \\ &\quad \times \left\{ 1 - \exp \left(- \int dm \frac{dn}{dm} [V(m) - V_o(m)] \right) \right\}^2, \end{aligned} \quad (17)$$

where we have taken the continuum limit for m and now make the explicit connection with the bubble mass. For clarity of presentation, we have suppressed the r_{12} dependence of $V_o(m)$. This function can be written explicitly as

$$V_o(m, r_{12}) = \begin{cases} 4\pi R^3(m)/3 - \pi r_{12}[R^2(m) - r_{12}^2/12], & r_{12} < 2R(m) \\ 0, & r_{12} > 2R(m). \end{cases} \quad (18)$$

Here $R(m)$ is the radius of an ionized region of mass m .

Equation (17) manifestly obeys all of the limits that we expect, and in particular ξ_{xx} is identically zero when $\bar{x}_i = 1$. However, it does not treat the overlap of H II regions correctly. We expect that when two ionized regions overlap, they expand so as to conserve volume (because the number of ionizing photons has not changed). The above prescription does *not* conserve volume. To solve this problem, we multiply the number density by $[-\ln(1 - \bar{Q})/\bar{Q}]$. We thus force $\bar{x}_i = \zeta f_{\text{coll}}$. Note that, provided we assign the bubble size distribution in such a manner that already includes overlap – such as that of equation (7) – we would ideally like to avoid *any* overlap when constructing the power spectrum. There is no clean way to avoid this problem, however, and our solution is a reasonable one.

3.3. Clustering

The treatment of §3.2 assumes that the ionized regions are uncorrelated on large scales. We can see this in equation (17) by noting that, when $V_o(m) \approx 0$, $\langle x_1 x_2 \rangle \rightarrow \bar{x}_i^2$. Thus the correlation function vanishes on scales larger than the bubble size. We now show how to include (approximately) the correlations between the bubbles induced by density modulations. Unfortunately, the precise clustering properties are difficult to determine because we only compute the probability that a point is ionized by *any* source; the root of the difficulty is that multiple sources can ionize a single point in our development, and it is not clear how to treat this possibility. However, the following simplification suffices for our purposes. We replace one of the factors in the last term of equation (17) by

$$\left\{ 1 - \exp \left(- \int dm \frac{dn}{dm} [V - V_o] [1 + \bar{\xi}(r_{12}, m)] \right) \right\}. \quad (19)$$

Here, $\bar{\xi}(r_{12}, m)$ is the excess probability that the point \mathbf{r}_2 is ionized by a source of size m given that \mathbf{r}_1 is ionized. Thus ξ is implicitly an average over all the sources able to ionize the first point. It is also approximate in that we have neglected the variation of the correlation function across $V(m)$. We are thus assuming that such variation is small, or that $r \gg R$. Fortunately, this is precisely the regime we are interested in: for small r , $[V(m) - V_o(m, r)] \rightarrow 0$ and the correlations are strongly suppressed anyway. This is a manifestation of the fact that we care only if a point is ionized at all, not whether it is ionized by a single or many sources.

We now assume that the correlation function can be written

$$\bar{\xi}(r, m) = \bar{b} b(m) \xi_{\delta\delta}(r), \quad (20)$$

where $\xi_{\delta\delta}(r)$ is the correlation function of the dark matter, $b(m)$ is the linear bias of a source of mass m , and

$$\bar{b} = \bar{Q}^{-1} \int dm b(m) V(m) \frac{dn}{dm} \quad (21)$$

is the bias averaged over the bubble filling factor. The weighting by V enters because the probability that our point is ionized by an object of size m is proportional to the object's volume. Finally, Sheth & Tormen (2002) have shown that the

bias of halos whose mass function is fixed by a linear barrier is

$$b(m, z) = 1 + \frac{B_0(z)^2}{\sigma^2(m) B(m, z)}. \quad (22)$$

For $\bar{x}_i \lesssim 0.5$, the bias factor is of order unity. However, it can become quite large near overlap. This is because the characteristic bubble size is fixed by $B \sim B_0 \sim \sigma$; thus the second term is $\sim 1/B(m, z)$ which is large near overlap. (At overlap, $B \approx 0$ so that the entire universe is ionized.) However, the correlations between bubbles in this regime turn out not to be significant. The typical correlation length at high redshifts is $\lesssim 1$ Mpc; once the characteristic bubble size exceeds this level the correlations can be neglected on the scales of interest (see §4.1 below).

3.4. Cross-Correlation with Density

The final step is to compute the cross-correlation between the density and ionization fields. If we use the halo model for the density field, this is straightforward:

$$\begin{aligned} \langle x_i(\mathbf{r}_1) \delta(\mathbf{r}_2) \rangle = & -\bar{x}_i + \int dm_h \frac{m_h}{\bar{\rho}} n_h(m_h) \int d^3 \mathbf{r}_h u(\mathbf{r}_2 - \mathbf{r}_h | m_h) \\ & \times \left\{ 1 - \exp \left[- \int dm_s \frac{dn}{dm_s} \right. \right. \\ & \left. \left. \times \int_{V(m_s, \mathbf{r}_1)} d^3 \mathbf{r}_s (1 + \xi_{m_s, m_h}(\mathbf{r}_h - \mathbf{r}_s)) \right] \right\}, \end{aligned} \quad (23)$$

where $n_h(m_h)$ is the halo mass function, ξ_{m_s, m_h} is the excess probability of having a bubble of size m_s given a halo of mass m_h at the specified separation, and $u(\mathbf{x} | m_h)$ is the normalized halo mass profile: $\int d^3 \mathbf{x} u(\mathbf{x} | m_h) = 1$ (Cooray & Sheth 2002).

As written, this is a quadruple integral that is difficult to evaluate numerically. Fortunately, we can make several straightforward simplifications. First, we again write the correlation function as a multiple of the dark matter correlation: $\xi_{m_s, m_h} \approx b(m_s) b_h(m_h) \xi_{\delta\delta}$, where $b_h(m_h)$ is the usual halo bias (Mo & White 1996). Second, we note that halos at high z are much smaller than both the bubble size and the separations that we are interested in. Thus we can set $\mathbf{r}_h \approx \mathbf{r}_2$ in the exponential. The integration over the mass profile is then separable (and equal to unity). Finally, we note that with this approximation the average of the correlation coefficient (i.e., the integral over \mathbf{r}_s) is also separable. We define

$$\langle \xi \rangle = \int dm \frac{dn}{dm} b(m) \int_{V(m, \mathbf{r}_1)} d^3 \mathbf{r}_s \xi_{\delta\delta}(|\mathbf{r}_s - \mathbf{r}_2|), \quad (24)$$

where the integral over $d^3 \mathbf{r}_s$ is centered on the point \mathbf{r}_1 . The limiting behavior of $\langle \xi \rangle$ is easy to understand. If the separation is much smaller than the characteristic bubble size R , the integral will be dominated by sources at typical separations R and $\langle \xi \rangle \sim \bar{b} \bar{Q} \xi_{\delta\delta}(R)$; if on the other hand $r \gg R$, the integral is dominated by sources at separations $r \approx r_{12}$ and $\langle \xi \rangle \sim \bar{b} \bar{Q} \xi_{\delta\delta}(r)$.

With these two simplifications, we can rewrite equation (23) as

$$\langle x_1 \delta_2 \rangle = (1 - \bar{x}_i) \left\{ 1 - \int dm_h \frac{m_h}{\bar{\rho}} n_h(m_h) e^{-b_h(m_h) \langle \xi \rangle} \right\}. \quad (25)$$

The limiting behavior of the cross-correlation is also easy to compute. We find that on large scales

$$\langle x_i(\mathbf{r}_1) \delta(\mathbf{r}_2) \rangle \approx (1 - \bar{x}_i) \bar{b}_h \bar{b} \bar{Q} \xi_{\delta\delta}(r_{12}), \quad r_{12} \gg R \quad (26)$$

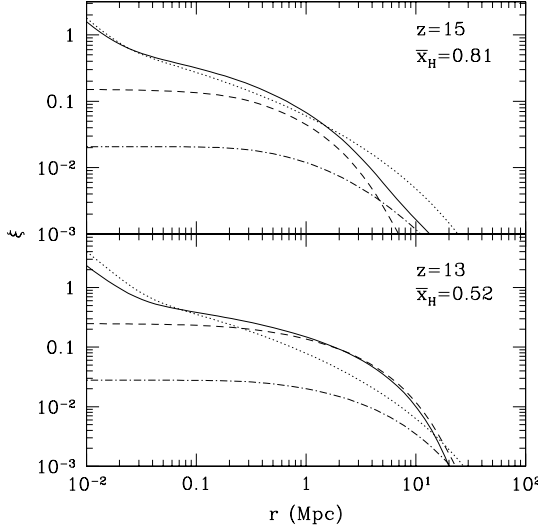


FIG. 5.— The correlation functions at $z = 15$ (top panel) and $z = 13$ (bottom panel), assuming that $\zeta = 40$. In each panel, the solid, dashed, dotted, and dot-dashed curves show ξ_ψ , ξ_{xx} , $\xi_{\delta\delta}$, and $|\xi_{x\delta}|$, respectively. (Note that the x_H and density fields are anticorrelated, so $\xi_{x\delta} < 0$.)

where \bar{b}_h is the mean halo bias (appropriately weighted) and R is the typical bubble size. We see that x_i and the density are positively correlated on large scales, with a constant correlation coefficient. This happens because we associate ionized regions with overdensities. On small scales,

$$\langle x_i(\mathbf{r}_1)\delta(\mathbf{r}_2) \rangle \approx (1 - \bar{x}_i)[1 - e^{-\bar{b}_h \bar{b} \bar{Q} \xi_{\delta\delta}(R)}], \quad r_{12} \ll R. \quad (27)$$

Thus for small separations the two fields are essentially uncorrelated so long as $\xi_{\delta\delta}(R)$ is not large; this is because the entire bubble is ionized in our model, regardless of its internal density structure.

Finally, note that in this section we have computed the cross-correlation between the ionized fraction and the density field. However, in equation (11) we want the cross-correlation between the *neutral* fraction and the density field. This is obviously $\xi_{x\delta} = -\langle x_i(\mathbf{r}_1)\delta(\mathbf{r}_2) \rangle$, so x_H and the density are anticorrelated.

4. RESULTS

4.1. The Correlation Function

We begin by describing the salient features of the correlation function, ξ_ψ . Figure 5 shows example correlation functions of density, x_H , and ψ at $z = 15$ (top panel) and $z = 13$ (bottom panel). Both assume $\zeta = 40$, which yields $\bar{x}_H = 0.81$ and 0.52 at these two redshifts. We also show the absolute value of the cross-correlation $\xi_{x\delta}$. First, we see that as r decreases from infinity, $\xi_{\delta\delta}$ first becomes shallow and then steepens again at small separations. The steepening occurs when the one-halo term becomes important; generally, this is on scales smaller than we will be able to probe with the next set of low-frequency radio telescopes.⁹

We can also see that ξ_{xx} has the form expected. At small separations, the correlation is dominated by whether the two points are in a single bubble or not; in this regime $\xi_{xx} \rightarrow$

⁹ The halo model correlation function in this regime also depends on the choice of halo mass function; we use the Press & Schechter (1974) mass function. The Sheth & Tormen (1999) mass function changes the one-halo term by $\lesssim 20\%$ here.

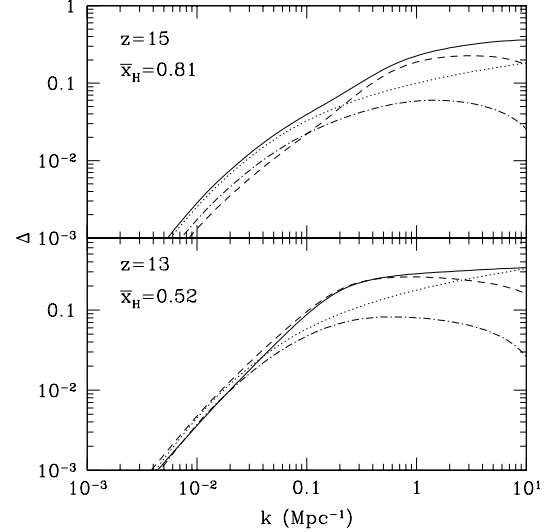


FIG. 6.— The power spectra at $z = 15$ (top panel) and $z = 13$ (bottom panel), assuming that $\zeta = 40$. In each panel, the solid, dashed, dotted, and dot-dashed curves show P_ψ , P_{xx} , $x_H^2 P_{\delta\delta}$, and $|P_{x\delta}|$, respectively. (Note that the x_H and density fields are anticorrelated, so $P_{x\delta} < 0$.)

$\bar{x}_H(1 - \bar{x}_H)$. At large separations, the points must each be inside different bubbles, so $\xi_{xx} \rightarrow 0$; actually the clustering term begins to dominate on sufficiently large scales and $\xi_{xx} \propto \xi_{\delta\delta}$ (this is just visible in the top panel). The transition between these two regimes occurs sharply, on scales that are comparable to the typical size of H II regions. In this intermediate regime we can have $\xi_{xx} \gg \xi_{\delta\delta}$, provided that the bubbles are sufficiently common and that the typical bubble size is significantly larger than the correlation length of the density field. (If not, ξ_{xx} simply traces the correlation function of the density field as it falls.) The cross-correlation has similar behavior, approaching a constant value at small separations and a constant multiple of ξ_{xx} on large scales. Note that the cross-correlation is negligible on small scales, essentially because our bubbles have no internal structure, but it can be important on large scales.

The solid lines in Figure 5 are ξ_ψ . On sufficiently small scales the dominant term in equation (11) is $\xi_{xx}\xi_{\delta\delta}$, and the correlation function is simply proportional to the one-halo term of the density field. On extremely large scales, ξ_ψ falls below $\xi_{\delta\delta}$ because of the anti-correlation between density and x_H . On intermediate scales, the ionized regions add only a small perturbation to ξ_ψ when the neutral fraction is large, but dominate by a large factor in the later stages of overlap. This “hump” is the observational signature that we seek.

4.2. The Power Spectrum

Figure 6 shows the power spectra of the correlation functions in Figure 5. Here $\Delta^2(k) = (k^3/2\pi^2)P(k)$ is the dimensionless power spectrum; we show the square root of this quantity because in 21 cm studies $\delta T \propto \psi$ rather than ψ^2 . The behavior is essentially as expected from the discussion of the correlation functions above. When the neutral fraction is large, P_ψ traces the density power spectrum, with the ionized regions adding only a small perturbation on the relevant scales. On large scales, P_ψ also traces the density power spectrum, but $P_\psi < P_{\delta\delta}$ because the bubbles are anti-correlated with density. Once overlap has become significant, P_{xx} dom-

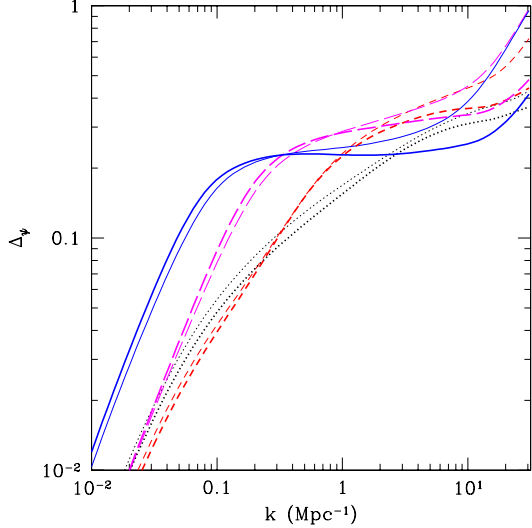


FIG. 7.— The redshift evolution of Δ_ψ in the $\zeta = 12$ (thin lines) and $\zeta = 40$ (thick lines) models. The curves are: $\bar{x}_H = 0.96$ (dotted), $\bar{x}_H = 0.8$ (short-dashed), $\bar{x}_H = 0.5$ (long-dashed), and $\bar{x}_H = 0.26$ (solid). The redshifts in the two models differ.

inates the power spectrum. In the bottom panels, the bubbles increase the power on and above their characteristic scale by nearly an order of magnitude. On large scales, our model predicts that P_ψ stops tracing $P_{\delta\delta}$ when \bar{x}_H is small. This is because the characteristic bubble size approaches infinity near overlap. The number density of the bubbles thus decreases rapidly when \bar{x}_H is small, so the “shot noise” becomes significant and dominates the large scale power. In this regime, $\Delta_\psi^2 \propto k^3$, which is approximately satisfied at $k \lesssim 0.1 \text{ Mpc}^{-1}$ in the bottom panel of Figure 6.

This Poisson noise component is to some extent an artifact of the simplifying assumptions inherent to our model. We assumed that each point is either fully ionized or fully neutral, neglecting effects like recombination, clumpiness, shadowing, asphericity, etc. Once the H II regions become sufficiently large, these effects will determine the internal structure of the bubbles. By effectively decreasing the size and increasing number density of ionized regions, they would therefore reduce the power on large scales, bringing P_ψ closer to the density power spectrum. Including these detailed effects will require numerical simulations.

We note that the power spectra shown here differ from those of ZFH04 in that the “bubble” feature is significantly less pronounced. This is simply because that paper employed a “toy” model in which the bubbles had a single effective size at each redshift. Also, our models have relatively more power on large scales late in reionization, because the ZFH04 analysis reduced the bubble size at these stages while keeping the number density fixed. Because the shot noise decreases with the number density, the large scale power was small in that case.

4.3. Reionization Histories

We now consider how the power spectrum evolves with time for some simple reionization histories. We will examine only single reionization episodes here, although our formalism can accommodate other, more complicated histories as well (see Furlanetto et al. 2004b). For reference, we note that

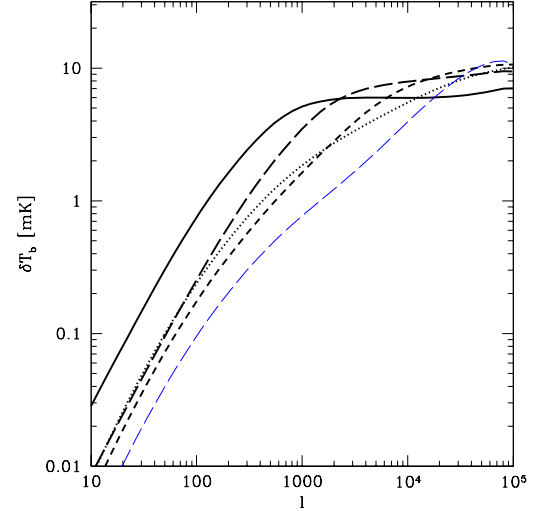


FIG. 8.— The angular power spectrum of brightness fluctuations in the $\zeta = 40$ model. The thick curves are for: $\bar{x}_H = 0.96$ (dotted), $\bar{x}_H = 0.8$ (short-dashed), $\bar{x}_H = 0.5$ (long-dashed), and $\bar{x}_H = 0.26$ (solid). The thin long-dashed curve is for the model where galaxies host their own individual HII regions ($\bar{x}_H = 0.5$).

a “typical” Population II star formation history, with $f_{\text{esc}} = 0.2$, $f_\star = 0.05$, $N_{\gamma/b} = 3200$, and $n_{\text{rec}} = 3$, would have $\zeta \approx 12$. This gives a reionization history similar to that of Sokasian et al. (2003a), who adopted a Population II star formation rate based on numerical simulations (Hernquist & Springel 2003; Springel & Hernquist 2003). Population III stars can have ζ an order of magnitude larger without much difficulty. The evolution of \bar{x}_H for some sample histories is illustrated in Figure 3.

Figure 7 shows the evolution of the power spectrum for $\zeta = 40$ (thick lines) and $\zeta = 12$ (thin lines). The dotted, short-dashed, long-dashed, and solid curves have $\bar{x}_H = 0.96, 0.8, 0.5$, and 0.25 , respectively. These correspond to $z \approx 18, 15, 13$, and 12 (for $\zeta = 40$) and $z \approx 16, 12, 10$, and 9 (for $\zeta = 12$). The most important point is that the power spectrum evolves substantially throughout reionization. While \bar{x}_H declines (and hence so does the mean brightness temperature for 21 cm observations), the H II regions add power and more than compensate for the paucity of neutral gas. Thus we confirm that statistical measurements can yield strong constraints on the ionization history. Surprisingly, the two curves show very little difference on scales $k \lesssim 10 \text{ Mpc}^{-1}$. The amplitudes, and especially the peak locations, closely match each other. On such scales the ionized regions dominate the power spectrum, so this indicates that the bubble size distribution for a fixed \bar{x}_H and m_{min} is nearly independent of redshift and ζ . In other words, the barrier $B(m, z)$ is determined primarily by the neutral fraction. This points to an interesting result of our model: when scaled to the global neutral fraction, the morphology of reionization does not vary strongly. The invariance does break down if ζ is extremely large (greater than several hundred) or if m_{min} is large. This is because the ionization field becomes more sensitive to the highly-biased peaks in such cases. It also breaks at small scales, where $P_\psi \propto P_{\delta\delta}$, because the latter grows rapidly in this redshift range. Finally, we caution the reader that the behavior on large scales during the late stages of reionization is not well-described by our

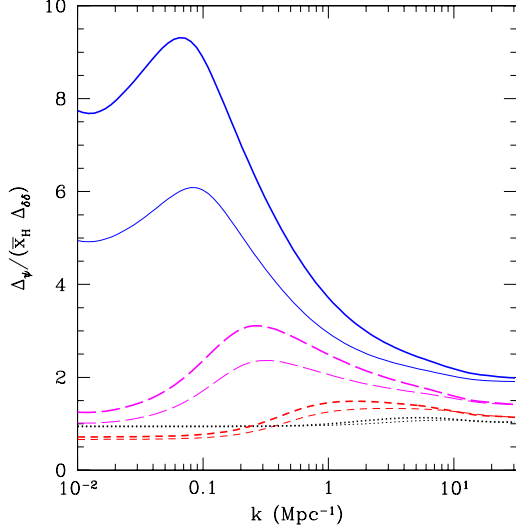


FIG. 9.— The redshift evolution of $\Delta_\psi / (\bar{x}_H \Delta_{\delta\delta})$ in the $\zeta = 12$ (thin lines) and $\zeta = 40$ (thick lines) models. The curves are: $\bar{x}_H = 0.96$ (dotted), $\bar{x}_H = 0.8$ (short-dashed), $\bar{x}_H = 0.5$ (long-dashed), and $\bar{x}_H = 0.26$ (solid). The redshifts in the two models differ.

model (see §4.2). Thus the trends we note may not hold in more detailed models near overlap.

In Figure 8 we show the angular power spectrum of the brightness fluctuations, which measures the root mean square level of fluctuations as a function of multipole l (see ZFH04 for details). To produce the figure we assumed that the observations were done with perfect frequency resolution.¹⁰ In that case, the angular power spectrum traces $\Delta_\psi(k)$ with the correspondence $l \sim kD$, where D is the angular diameter distance to the appropriate redshift. As a result, all the features in Figure 7 can be seen in Figure 8. For an experiment with finite resolution the power spectra will be somewhat different on small angular scales. An observed bandwidth $\Delta\nu$ corresponds to a comoving distance

$$L \approx 1.7 \left(\frac{\Delta\nu}{0.1 \text{MHz}} \right) \left(\frac{1+z}{10} \right)^{1/2} \left(\frac{\Omega_m h^2}{0.15} \right)^{-1/2} \text{Mpc.} \quad (28)$$

We denote by $l_{\Delta\nu}$ the multipole corresponding to the angle subtended by L . The angular power spectrum will be given by $\Delta_\psi(l/D)$ for $l < l_{\Delta\nu}$, but will be proportional to $\Delta_\psi(l/D) \times (l_{\Delta\nu}/l)$ for $l > l_{\Delta\nu}$. Thus, on small angular scales the shape of the spectrum will change and the fluctuations will be reduced. For frequency resolutions around $\Delta\nu \sim 0.2$ MHz, realistic for upcoming experiments, this change in behavior will happen at arcminute scales, or equivalently $l \sim 10^4$ (see ZFH04 for details).

The behavior on small scales is better understood through Figure 9, which shows the ratio between ψ in our model and that of a uniformly ionized IGM with the same \bar{x}_H . At large k , the curves each approach constant values nearly independent of ζ . That is, P_ψ is nearly proportional to $P_{\delta\delta}$ at large wavenumbers. In fact, it is easy to see from equation (11) that $P_\psi / P_{\delta\delta} \sim \bar{x}_H$. (There is actually an additional bias factor that affects the limiting value.) Figure 9 also shows explicitly that the bubble peak moves to larger scales and higher amplitude as reionization progresses. At a fixed neutral fraction,

¹⁰ We have also neglected redshift space distortions; see ZFH04 for a discussion of their importance.

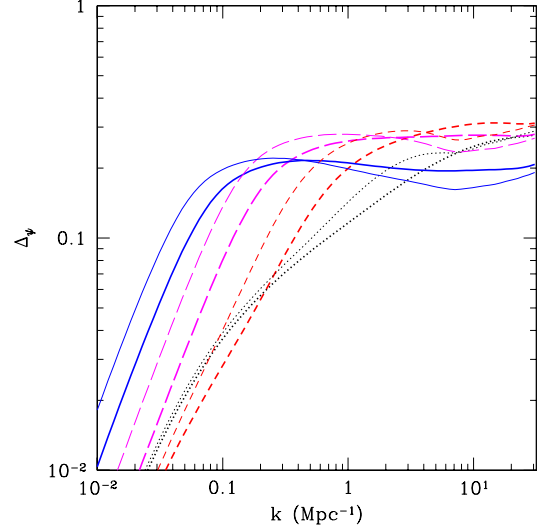


FIG. 10.— The redshift evolution of Δ_ψ in the $\zeta = 500$ (thin lines) and $\zeta = 90$ (thick lines) models. In the latter case, we decrease m_{\min} by an order of magnitude from the default model. The curves are: $\bar{x}_H = 0.96$ (dotted), $\bar{x}_H = 0.8$ (short-dashed), $\bar{x}_H = 0.5$ (long-dashed), and $\bar{x}_H = 0.24$ (solid). The redshifts in the two models differ slightly.

the peak amplitude relative to the underlying density field is largest at early times. This is partly because the large scale bubble characteristics are nearly independent of redshift while the density power spectrum grows as $(1+z)^{-1}$ and partly because the bias increases with redshift. Thus (from a theoretical standpoint) distinguishing between a uniformly ionized medium and one with fully ionized regions will be somewhat easier if reionization occurs earlier.

Figure 10 compares two early reionization scenarios in which overlap is complete by $z \sim 16$. The thin lines assume $\zeta = 500$ and the usual value of m_{\min} ; the thick lines have $\zeta = 90$ but decrease m_{\min} by a factor of 10. The redshifts in the Figure are slightly different, ranging from $z = 22.5$ – 17.2 in the $\zeta = 500$ model and $z = 24$ – 17 in the other. As one might expect from the above discussion, there is relatively little difference between the two histories, at least in terms of the power spectra. Our model predicts that features occur on slightly larger angular scales for $\zeta = 500$ and have slightly less small-scale power. The bubble feature also appears earlier in the $\zeta = 500$ model. This is because the bubbles are initially significantly larger in this case (both because the sources are stronger and because they are more rare). However, overall the differences are small enough that distinguishing them will probably require a more accurate treatment of reionization through numerical simulations. When compared to Figure 7, the major difference is the increased large scale power. This too is because the H II regions have a smaller number density and hence the shot noise term becomes significant earlier.

4.4. H II Regions Around Individual Galaxies

The formalism described in §3 is general and does not rely on our model for the size distribution of H II regions. We can thus apply it to a scenario in which each galaxy hosts its own ionized region; the size distribution is then shown in the top panel of Figure 4. Such a model would be relevant if galaxies were truly randomly distributed. Figure 11 shows the power spectra for several redshifts, again assuming $\zeta = 40$. These curves can therefore be compared directly to the thick lines

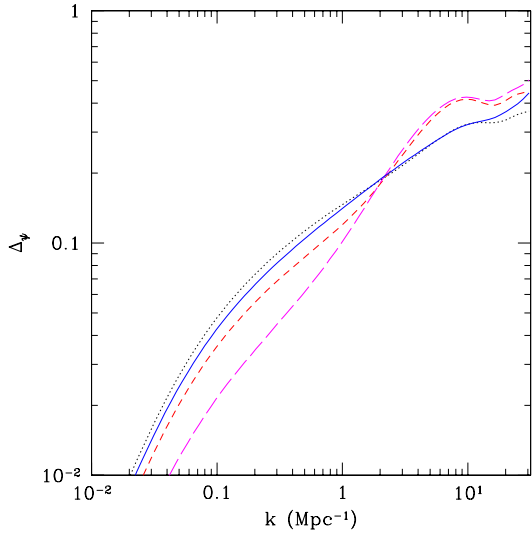


FIG. 11.— The redshift evolution of Δ_ψ if we assume that each galaxy hosts its individual H II region. All curves assume $\zeta = 40$. The lines are: $\bar{x}_H = 0.96$ (dotted), $\bar{x}_H = 0.8$ (short-dashed), $\bar{x}_H = 0.5$ (long-dashed), and $\bar{x}_H = 0.26$ (solid).

in Figure 7. The difference between the models is substantial and it can also be seen in the angular power spectrum (see Figure 8). First, in the present case the peak not only occurs at smaller scales, but its location does not shift significantly as reionization is approached. This is because overlap is achieved not by increasing the sizes of individual galaxies (though that does slowly happen) but instead by rapidly increasing their number density. Second, the large scale behavior is significantly different: in the present case $P_\psi \propto P_{\delta\delta}$, and is always *smaller* than the power assuming a fully neutral medium. This is because the number of ionized regions is so large, making the shot noise negligible. The large scale power is minimized when $\bar{x}_H \approx 0.5$, because at that point the (anti-correlated) density and x_H fields nearly cancel each other out. The long-dashed thin curve in Figure 8 shows the corresponding angular power spectrum for this model with $\bar{x}_H = 0.5$. We see that δT_b is nearly featureless on scales $l \lesssim 10^4$, with the bubbles appearing only at sub-arcminute scales. There is also a significant deficit of large-scale power. This comparison emphasizes the importance of considering large H II regions when describing reionization.

5. THE PIXEL DISTRIBUTION FUNCTION & NON-GAUSSIAN SIGNATURES

The power spectrum that we have computed in the last two sections is only one statistical characterization of the maps. Its widespread use in many studies, and in particular for the CMB and galaxy redshift surveys, stems from the fact that linear density perturbations are nearly gaussian. For such a field, the power spectrum completely describes its statistical properties. In our case, however, the ionization pattern is not gaussian, so other characterizations may be more powerful. Here, we estimate the expected probability distribution function (PDF) of the dimensionless pixel neutral hydrogen density ψ with an eye toward developing such alternative diagnostics. We caution the reader that this treatment will only be approximate; more sophisticated techniques, and probably numerical simulations, will be required for accurate descriptions.

We begin by selecting our pixel size and the effective enclosed mass m_{pix} (assuming the mean density for the volume-to-mass conversion). Conceptually, we divide the H II regions into those larger than m_{pix} and those smaller than this mass scale. The PDF will have two components: a delta function at $\psi = 0$ made up of the large bubbles and a broader distribution at $\psi > 0$ composed of pixels with a mix of neutral gas and small bubbles. We can construct the second component as follows.

Suppose we select a region with smoothed overdensity δ_0 . We first assume that the density field is gaussian; this is a reasonable approximation on most of the scales of interest (see below). Then we know $f_{\text{coll}}(\delta_0)$ and hence also $\psi(\delta_0)$ provided that we include only sources contained inside this pixel. If these were the only relevant ionizing sources, we could construct the PDF of ψ in the usual way: $p(\psi) = p(\delta)|d\delta/d\psi|$. However, we must also account for ionizing sources outside of our selected region; in other words, we need the probability that a pixel with a given δ_0 is contained within one of the large bubbles. In terms of the excursion set formalism, we wish to compute the probability that a particular trajectory that passes through our pixel scale at the appropriate density has passed above our barrier $B(\sigma^2)$ for some $\sigma^2 < \sigma_{\text{pix}}^2$; i.e., that it has been incorporated into a large-scale H II region. We let $p(\delta_\sigma^f = B_\sigma | \delta_{\sigma_{\text{pix}}} = \delta_0)$ be the conditional probability that a trajectory first crosses the barrier at σ^2 given that it has $\delta(\sigma_{\text{pix}}^2) = \delta_0$. The total probability that our pixel is fully ionized is then

$$p_i(\delta_0) = \int_0^{\sigma_{\text{pix}}^2} d\sigma^2 p(\delta_\sigma^f = B_\sigma | \delta_{\sigma_{\text{pix}}} = \delta_0). \quad (29)$$

To compute the integrand, we use Bayes' Theorem:

$$\begin{aligned} p(\delta_\sigma^f = B_\sigma | \delta_{\sigma_{\text{pix}}} = \delta_0) &= \\ p(\delta_{\sigma_{\text{pix}}} = \delta_0 | \delta_\sigma^f = B_\sigma) p(\delta_\sigma^f = B_\sigma). \end{aligned} \quad (30)$$

Here $p(\delta_{\sigma_{\text{pix}}} = \delta_0 | \delta_\sigma^f = B_\sigma)$ is the conditional probability that a trajectory has δ_0 on our pixel scale given that it first crosses the barrier at σ^2 . This, as well as $p(\delta)$, are gaussian, while $p(\delta_\sigma^f = B_\sigma)$ is the first-crossing distribution described in §2. Thus

$$\begin{aligned} p(\delta_\sigma^f = B_\sigma | \delta_{\sigma_{\text{pix}}} = \delta_0) &= \frac{B}{\sqrt{2\pi}} \frac{\sigma_{\text{pix}}}{\sigma^3(\sigma_{\text{pix}}^2 - \sigma^2)^{1/2}} \\ &\times \exp \left[-\frac{(\delta\sigma^2 - B\sigma_{\text{pix}}^2)^2}{2\sigma^2\sigma_{\text{pix}}^2(\sigma_{\text{pix}}^2 - \sigma^2)} \right]. \end{aligned} \quad (31)$$

If we instead used a constant barrier, note that p_i could be written explicitly using mirror symmetry about the barrier, as in the standard derivation of the Press-Schechter mass function (Bond et al. 1991).

The PDF of ψ is then simply

$$p(\psi) = \sum_{i=1}^2 p(\delta_i) \left| \frac{d\delta}{d\psi} \right|_{\delta_i} [1 - p_i(\delta_i)]. \quad (32)$$

The summation occurs because $\psi(\delta)$ is not monotonic. Clearly ψ approaches zero as the density decreases. But it also approaches zero as $\delta \rightarrow \infty$. At high densities, more ionizing sources reside in the pixel and x_H approaches zero. Thus, ψ has a maximum value ψ_{max} at any pixel size and redshift, and any given ψ corresponds to two densities δ_i . Also note that the PDF becomes singular (though still integrable) at ψ_{max} .

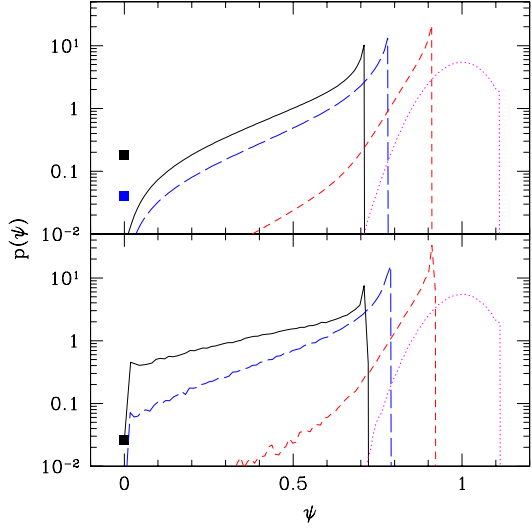


FIG. 12.— The probability distribution $p(\psi)$ for $m_{\text{pix}} = 10^{13} \text{ M}_\odot$ and $\zeta = 40$. Dotted, short-dashed, long-dashed, and solid curves are for $z = 20, 16, 14$, and 13 , respectively. The top panel shows the PDF of equation (32), while the bottom panel approximately includes overlap with large bubbles (see text). The filled squares indicate the total probability of the pixel being fully ionized. In the top panel, the upper and lower squares are $z = 13$ and $z = 14$, respectively; in the lower panel, only $z = 13$ has a non-negligible probability.

For analytic studies, it can thus be easier to consider the cumulative distribution function, $P(>\psi)$, which is always non-singular.

Some examples are shown in Figure 12. We choose $m_{\text{pix}} = 10^{13} \text{ M}_\odot$, corresponding to $R \approx 3.9 \text{ Mpc}$ or an angular diameter $\theta \approx 2.7'$ at $z = 13$. The top panel shows $p(\psi)$ at $z = 20, 16, 14$, and 13 (dotted, short-dashed, long-dashed, and solid curves, respectively) in the $\zeta = 40$ model. At $z = 20$, the PDF resembles a truncated gaussian. But even at $z = 16$, when $\bar{x}_H = 0.88$, ionizations have completely transformed the shape of the PDF. As described above, this is because the higher density regions have larger f_{coll} and hence smaller neutral fractions. The high tail of the density distribution is thus folded over around ψ_{max} (which corresponds to $\delta \sim 0$). Moreover, when the density is close to the mean value, x_H is nearly linear in the overdensity, so the peak can be quite sharp. As the bubbles grow, the peak shifts to smaller ψ and the tail grows rapidly. This occurs because high-density pixels have a higher probability of being mostly ionized by bubbles comparable to their own size. Once the characteristic bubble size passes m_{pix} (which happens just before $z = 13$ for these parameters, see Figure 2), the probability of $\psi = 0$ rises rapidly as well.

Another way to look at this is through $P(>\psi)$, which we show in Figure 13. The solid curves are for the above model, while the dotted curves show the same function for a uniformly ionized universe. (In the latter case the PDF is just a gaussian.) The curves are for $z = 20, 16, 14$, and 13 , from top to bottom. We see clearly that even when the ionized fraction is only a few percent, the high-density tail is truncated and folded over to add to the small- ψ component. It is obvious from this figure that the variance is *smaller* in the f_{coll} model during the early phases of reionization; this is again because high density regions and ionized bubbles are strongly correlated. However, as the bubbles grow $P(\psi)$ rapidly spreads toward $\psi = 0$; this corresponds to fluctuations in the ionized

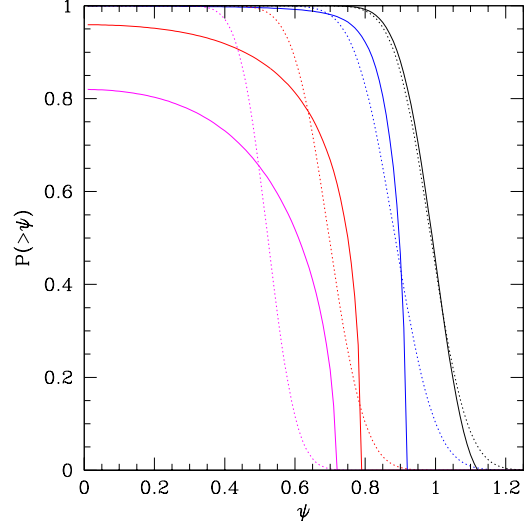


FIG. 13.— The cumulative distribution function of ψ , assuming $m_{\text{pix}} = 10^{13} \text{ M}_\odot$ and $\zeta = 40$. The solid curves assume our model, while the dotted curves assume a uniformly ionized medium. In each case, the curves are for $z = 20, 16, 14$, and 13 , from top to bottom.

fraction dominating the power spectrum. This figure also explicitly shows that the probability of having a fully ionized region is negligible until $z \sim 13$.

This version of the PDF is not necessarily the natural choice for comparing to observations, because we have assigned all of the large bubbles to pixels with zero flux. In a real survey, pixels could intersect a fraction of a bubble. In the limits in which the characteristic bubble size is either much smaller or much larger than the pixel size, this complication can be neglected. We can estimate the PDF in the intermediate range if we assume (i) that the fully ionized part of a pixel is uncorrelated with the mean density of the rest of the pixel, and (ii) that the part outside of a large bubble follows the distribution of equation (32); we thus neglect the fact that this component is smaller than the full pixel size. In this case, the only additional component we need is the distribution of the fraction f_i of the pixel that is inside of large ionized bubbles. This can be written

$$p(f_i > f_0) = 1 - \exp \left[- \int dm \frac{dn}{dm} V_{\text{max}}(m, f_0) \right], \quad (33)$$

where $V_{\text{max}}(m, f_0)$ is the volume within which a bubble of the specified mass will cover a fraction f_0 or larger of the pixel; it is a straightforward generalization of equation (18).

In this case we simulate $p(\psi)$ through a Monte Carlo algorithm. We randomly select both f_i and ψ_n using their respective cumulative distribution functions. Here, ψ_n refers to the part of the pixel outside of the large bubble, so $\psi = f_i \psi_n$. Some examples of $p(\psi)$ are shown in the bottom panel of Figure 12. The effects of overlap with fully ionized regions are obviously negligible when the pixel size is significantly larger than the typical bubble size. When the two scales are comparable at $z \sim 13$, overlap spreads the delta function at $\psi = 0$ out, but it does not qualitatively affect the results. If we had included correlations, the effect of overlap would be slightly smaller than shown here because pixels near ψ_{max} are less likely to be near ionized regions than pixels that are already mostly ionized.

We have assumed throughout this section that the density field has a gaussian distribution. This is obviously only relevant on scales where the power spectrum is approximately linear. Our approximation breaks down when higher moments of the density field become significant. As an example we consider the third moment of $p(\delta)$. The skewness due to pure gravitational instability is $\langle \delta^3 \rangle = S_3 \langle \delta^2 \rangle^2$, where $S_3 = [34/7 - (3+n)]$ if $P(k) \propto k^{-n}$ (Bouchet et al. 1992; Juszkiewicz et al. 1993). The skewness only becomes significant at $m \lesssim 10^{12} M_\odot$ for $z \gtrsim 10$, so our choice of m_{pix} is reasonable.

We thus see that the boosts in power from the H II regions are actually a result of a qualitative change in $p(\psi)$ and not simply an increase in the variance of a gaussian. This shows explicitly that exploring statistics beyond the power spectrum is crucially important to understanding the 21 cm signal. From the estimates we have made here, the optimal tests are not immediately obvious; we will defer closer examination to the future. Of course, our model is only approximate, as we treat the perturbations in Lagrangian rather than real space and neglect large-scale correlations and recombinations. All of these complications will be important in determining the true shape of the PDF and to what extent observations can distinguish different models, but none will change our general conclusion about the importance of non-gaussianity. For example, the shape of the PDF is determined entirely by our model for reionization; in other models with comparable power the PDF could still have a qualitatively different shape. We explore one such example in Furlanetto et al. (2004b).

6. DISCUSSION

In this paper, we have described a new analytic model for the size distribution of H II regions during reionization. While the overlap process is usually described in terms of Strömgren spheres around individual galaxies, recent cosmological simulations of reionization have demonstrated that the ionized regions are much larger than naively expected, even early in the reionization process. Here we have shown that the size distribution can be understood in terms of large-scale features in the density field, and we have constructed the size distribution with an approach analogous to the standard derivation of the Press & Schechter (1974) mass function for collapsed halos. The model has only two input parameters (if the cosmology is fixed): the ionizing efficiency of collapsed objects and the minimum mass halo that can host a luminous object. Interestingly, at a fixed neutral fraction the characteristic size of the bubbles is fairly insensitive to these input parameters, suggesting that the morphology of reionization is close to invariant (at least for simple, single reionization episodes). While we make several simplifying approximations in the model (see the discussion in §2), it provides a self-consistent approach that reproduces the qualitative features of simulations. In the future, the model must be quantitatively compared to simulations; however, an accurate comparison requires simulations with large ($\sim 100^3 \text{ Mpc}^3$) volumes because of the effects of the large-scale density field (see Figure 4, as well as Barkana & Loeb 2003).

The morphology of reionization has implications for a number of observables. Most important, regardless of the technique, we predict large H II regions that should be feasible to detect, whether through quasar absorption spectra (Miralda-Escudé et al. 2000; Barkana & Loeb 2002), Ly α lines at extremely high-redshifts (Pelló et al. 2004; Loeb et al. 2004; Ri-

otti et al. 2004; Gnedin & Prada 2004; Cen et al. 2004; Barton et al. 2004), or 21 cm tomography. For example, the noise in a 21 cm map is proportional to the square root of the bandwidth and, more important, to the square of the pixel size. Our model predicts substantial contrast on relatively large scales of several arcminutes, which should make detections easier. Note, however, that in many next-generation experiments like LOFAR the “bandwidth” can be chosen *after* the observations are complete, so the expected scale of the bubbles need not determine the experimental design (Morales & Hewitt 2003).

Even if high signal-to-noise detections of individual H II regions are not available, we have shown that statistical measurements of the size distribution can still strongly constrain reionization. We first constructed the power spectrum of fluctuations in the neutral density, including both density fluctuations and the ionized regions. We found that the ionized regions imprint clear features on the power spectrum and amplify the power by a factor of several during the middle and late stages of reionization. Most important, the power spectrum evolves throughout reionization, allowing us to map the time history of reionization. For 21 cm observations, the large-scale H II regions predicted by our model put the features at $l \lesssim 10^4$ (or $\theta \gtrsim 2'$). This matches well to the scales able to be probed by upcoming experiments like PAST, LOFAR, and SKA (ZFH04). If, on the other hand, reionization occurred through the overlap of H II regions around individual galaxies, the features in the power spectrum would appear at much smaller scales, perhaps beyond the reach of these instruments. We have also shown explicitly that the ionized bubbles induce qualitative changes to the initially gaussian neutral density distribution. This suggests that statistical measurements beyond the power spectrum can offer probes of the physics of reionization that may be even more powerful.

Our results also have important implications for other measurements. For example, one of the most successful strategies for targeting high-redshift galaxies is by searching for strong Ly α emitters. If the galaxy is embedded in a mostly neutral medium, Ly α absorption from the IGM can have a substantial effect on the line profile (Haiman 2002; Santos 2003; Loeb et al. 2004). In our model, we expect this absorption to be less significant, because most galaxies are embedded in H II regions with large sizes, even relatively early in the reionization process.

Finally, in this paper we have considered only the simplest reionization histories with a single type of source. Many models for reconciling the quasar and CMB data on reionization require multiple, distinct generations of sources that cause “stalling” or even “double” reionization (Wyithe & Loeb 2003; Cen 2003; Haiman & Holder 2003; Sokasian et al. 2003b). Such histories will of course change the morphology of reionization and hence modify the 21 cm signal. Moreover, alternative models of reionization in which (for example) voids are ionized first yield different sets of signatures. In Furlanetto et al. (2004b), we use the formalism developed here to examine how well 21 cm tomography can distinguish these histories and models.

This work was supported in part by NSF grants ACI AST 99-00877, AST 00-71019, AST 0098606, and PHY 0116590 and NASA ATP grants NAG5-12140 and NAG5-13292 and by the David and Lucille Packard Foundation Fellowship for Science and Engineering.

REFERENCES

Arons, J., & Wingert, D. W. 1972, *ApJ*, 177, 1

Barkana, R. 2002, *New Astronomy*, 7, 85

Barkana, R., & Loeb, A. 2001, *Phys. Rep.*, 349, 125

—. 2002, *ApJ*, 578, 1

—. 2003, *ApJ*, submitted, (astro-ph/0310338)

Barton, E.J., Davé, R., Smith, J.-D.T., Papovich, C., Hernquist, L. & Springel, V. 2004, *ApJ*, in press (astro-ph/0310514)

Becker, R. H., et al. 2001, *AJ*, 122, 2850

Bond, J. R., Cole, S., Efstathiou, G., & Kaiser, N. 1991, *ApJ*, 379, 440

Bouchet, F. R., Juszkiewicz, R., Colombi, S., & PELLAT, R. 1992, *ApJ*, 394, L5

Cen, R. 2003, *ApJ*, 591, L5

Cen, R., Haiman, Z., & Mesinger, A. 2004, *ApJ*, submitted, (astro-ph/0403419)

Ciardi, B., & Madau, P. 2003, *ApJ*, 596, 1

Ciardi, B., Stoehr, F., & White, S. D. M. 2003, *MNRAS*, 343, 1101

Cooray, A., & Sheth, R. 2002, *Phys. Rep.*, 372, 1

Di Matteo, T., Ciardi, B., & Miniati, F. 2004, *MNRAS*, submitted, (astro-ph/0402322)

Di Matteo, T., Perna, R., Abel, T., & Rees, M. J. 2002, *ApJ*, 564, 576

Fan, X., et al. 2002, *AJ*, 123, 1247

Field, G. B. 1958, *Proc. IRE*, 46, 240

—. 1959, *ApJ*, 129, 525

Fukugita, M., & Kawasaki, M. 2003, *MNRAS*, 343, L25

Furlanetto, S. R., Sokasian, A., & Hernquist, L. 2004a, *MNRAS*, 347, 187

Furlanetto, S. R., Zaldarriaga, M., & Hernquist, L. 2004b, *ApJ*, submitted

Gnedin, N. Y. 2000, *ApJ*, 535, 530

Gnedin, N. Y., & Prada, F. 2004, *ApJ*, submitted, (astro-ph/0403345)

Gnedin, N. Y., & Shaver, P. A. 2003, *ApJ*, submitted, (astro-ph/0312005)

Gunn, J. E., & Peterson, B. A. 1965, *ApJ*, 142, 1633

Haiman, Z. 2002, *ApJ*, 576, L1

Haiman, Z., & Holder, G. P. 2003, *ApJ*, 595, 1

Hernquist, L. & Springel, V. 2003, *MNRAS*, 341, 1253

Juszkiewicz, R., Bouchet, F. R., & Colombi, S. 1993, *ApJ*, 412, L9

Kogut, A., et al. 2003, *ApJS*, 148, 161

Lacey, C., & Cole, S. 1993, *MNRAS*, 262, 627

Loeb, A., Barkana, R., & Hernquist, L. 2004, *ApJ*, submitted, (astro-ph/0403193)

Madau, P., Meiksin, A., & Rees, M. J. 1997, *ApJ*, 475, 429

Miralda-Escudé, J., Haehnelt, M., & Rees, M. J. 2000, *ApJ*, 530, 1

Mo, H. J., & White, S. D. M. 1996, *MNRAS*, 282, 347

Morales, M. F., & Hewitt, J. 2003, *ApJ*, submitted, (astro-ph/0312437)

Oh, S. P., & Mack, K. J. 2003, *MNRAS*, 346, 871

Onken, C. A., & Miralda-Escudé, J. 2003, *ApJ*, submitted, (astro-ph/0307184)

Pelló, R., et al. 2004, *A&A*, 416, L35

Press, W. H., & Schechter, P. 1974, *ApJ*, 187, 425

Ricotti, M., Haehnelt, M. G., Pettini, M., & Rees, M. J. 2004, *MNRAS*, submitted, (astro-ph/0403327)

Santos, M. G., et al. 2003, *ApJ*, 598, 756

Santos, M. R. 2003, *MNRAS*, submitted, (astro-ph/0308146)

Scott, D., & Rees, M. J. 1990, *MNRAS*, 247, 510

Sheth, R. K. 1998, *MNRAS*, 300, 1057

Sheth, R. K., & Tormen, G. 1999, *MNRAS*, 308, 119

Sheth, R. K., & Tormen, G. 2002, *MNRAS*, 329, 61

Sokasian, A., Abel, T., Hernquist, L., & Springel, V. 2003a, *MNRAS*, 344, 607

Sokasian, A., Yoshida, N., Abel, T., Hernquist, L., & Springel, V. 2003b, *MNRAS*, in press (astro-ph/0307451)

Songaila, A. 2004, *AJ*, in press, (astro-ph/0402347)

Spergel, D. N., et al. 2003, *ApJS*, 148, 175

Springel, V., & Hernquist, L. 2003, *MNRAS*, 339, 312

Tozzi, P., Madau, P., Meiksin, A., & Rees, M. J. 2000, *ApJ*, 528, 597

White, R. L., Becker, R. H., Fan, X., & Strauss, M. A. 2003, *AJ*, 126, 1

Wyithe, J. S. B., & Loeb, A. 2003, *ApJ*, 588, L69

—. 2004, *Nature*, 427, 815

Zaldarriaga, M., Furlanetto, S. R., & Hernquist, L. 2004, *ApJ*, in press, (astro-ph/0311514) [ZFH04]